

Strain-induced interfacial hole localization in self-assembled quantum dots: Compressive InAs/GaAs versus tensile InAs/InSb

Lixin He, Gabriel Bester, and Alex Zunger*

National Renewable Energy Laboratory, Golden, Colorado 80401, USA

(Received 13 September 2004; published 15 December 2004)

Using an atomistic pseudopotential approach, we study how the shape of the dot (spherical vs lens shaped) affects the position-dependent strain and the electronic properties of tensile (InAs/InSb) and compressive (InAs/GaAs) quantum dots. We compare the strain profiles, strained modified band offsets, confined levels, and atomistic wave functions of these dots. We show (i) how the existence of position-dependent strain in nonflat heterostructures can control the electronic properties, leading, for example, to interfacial localization of hole states on the interface of matrix-embedded dots and (ii) how the dots shape can control the level sequence and degeneracy. For example in spherical dots, one finds degenerate light-hole (LH) and heavy-hole (HH) states, whereas in lens-shaped dots one can have as the highest-occupied hole state either (a) a LH state inside the dot, becoming a HH state outside the dot (InAs/InSb tensile case) or (b) a HH state inside the dot, becoming a LH states outside the dot (InAs/GaAs compressive case).

DOI: 10.1103/PhysRevB.70.235316

PACS number(s): 68.65.Hb, 73.22.-f

I. INTRODUCTION

Semiconductor heterostructures^{1,2} are often constructed from lattice-mismatched components (Si/Ge, InAs/GaAs, InAs/InSb). This leads, in general, to the creation of both isotropic (hydrostaticlike) strain $I = \epsilon_{xx} + \epsilon_{yy} + \epsilon_{zz}$, as well as biaxial strain $B = [(\epsilon_{xx} - \epsilon_{yy})^2 + (\epsilon_{yy} - \epsilon_{zz})^2 + (\epsilon_{zz} - \epsilon_{xx})^2]^{1/2}$, where $\epsilon_{\alpha\beta}$ are the $\alpha\beta$ -th components of the cubic strain tensor. Whereas such strain can limit the film thickness and planarity, it can also be used advantageously to engineer certain strain-induced electronic properties such as band gaps and subband splittings. In *flat* heterostructures, such as quantum wells or superlattices,^{1,2} both I and B are position independent. Recent advances in the growth of “self-assembled” systems³ have now made possible the fabrication of nonflat heterostructures, such as zero-dimensional quantum dots (QD’s), in which a dot of one material is coherently strained in a matrix of another material. It turns out⁴ that in such nonflat heterostructures the biaxial strain is a function of position, decaying with distance away from the interface. Such a behavior can modify the confining potential, leading to carrier localization.^{5,6} In the following, we show that biaxial strain (a) controls the heavy-hole (HH), light-hole (LH) degeneracy, (b) reverses the order of the HH and LH potentials inside and outside the dots, and (c) leads to interfacial hole localization.

II. SYSTEM STUDIED AND METHOD

We consider a case of a dot under tensile strain (InAs in InSb) as well as a dot under compressive strain (InAs in GaAs). Whereas tensile dots are not as popular as compressed dots,³ the former can be grown in the Stranski-Krastanov (SK) mode as demonstrated⁷ for PbSe-in-PbTe. We have considered for both systems spherical shape (obtained regularly in colloidal growth,^{8,9} albeit unstrained), and lens shape (obtained regularly in SK growth³). Although spherical dots cannot be grown in SK mode, it is very in-

structive to compare them with lens-shaped dots to gain better understandings of the shape effect. In all cases, we relax the strain using atomistic elasticity, minimizing the strain energy as a function of the coordinates of all the atoms, and representing the energy in terms of bond-bending and bond-stretching springs (the valence force field, or VFF model¹⁰). Once we find the relaxed positions $\{\mathbf{R}_{i,\alpha}\}$ of all (dot + matrix) atoms of type α at site i , we calculate the total electron-ion potential $V(\mathbf{r}) = V_{\text{SO}} + \sum_i \sum_\alpha v_\alpha(\mathbf{r} - \mathbf{R}_{i,\alpha})$ as a superposition of local screened atomic pseudopotential $v_\alpha(\mathbf{r})$, and the total (nonlocal) spin-orbit (SO) potential V_{SO} . Our atomistic pseudopotentials^{11,12} are fitted to all the physically important properties of the materials, including band energies at high-symmetry points, effective masses, strained band offsets, and hydrostatic and biaxial deformation potentials of individual band edges. The Hamiltonian $-1/2\nabla^2 + V(\mathbf{r})$ is diagonalized in a basis $\{\phi_{n,\epsilon}^{(\lambda)}(\mathbf{k})\}$ of Bloch orbitals of band index n and wave vector \mathbf{k} of material λ (=InAs, InSb, GaAs), strained uniformly to strain $\vec{\epsilon}$. For the InAs/InSb dots we used a basis set of $n=8$ bands (including spin) for each material on a $7 \times 7 \times 7$ k -point mesh around the Γ point. For the (unstrained) matrix material InSb, we generated these Bloch functions at $\vec{\epsilon}=0$, whereas for the strained dot material (InAs) we use the average $\vec{\epsilon}$ value obtained from VFF atomistic relaxation. For the InAs/GaAs, we use $n=6$ for the hole states, and $n=2$ for electron states on a $6 \times 6 \times 12$ k mesh. Again, we use $\vec{\epsilon}=0$ for the (unstrained) GaAs matrix material, and an average $\vec{\epsilon}$ value from VFF for the strained dot material (InAs). This approach of linear combination of Bulk Bands (LCBB)¹³ produces accurate results relative to an ordinary plane-wave basis at a fraction of the cost, and greatly surpasses^{14,15} in accuracy the $\mathbf{k} \cdot \mathbf{p}$ method³ which limits the basis to $n = \text{VBM} + \text{CBM}$ at $\mathbf{k}=0$ only and lacks atomistic symmetry.¹⁶ The pseudopotential used for the InAs/GaAs dots are identical to those used in Ref. 11, whereas for the InAs/InSb dots the potentials of Ref. 12 are used with a minor modification.¹⁷ Table I summarizes our

TABLE I. Summary of the results of strain profiles and confining potentials along [001] direction for spherical and lens-shaped QD's. I and B are the isotropic and biaxial strains, respectively. $E_g = V_{\text{CBM}} - V_{\text{VBM}}$, while V_{HH} and V_{LH} are the HH and LH confining potentials.

Properties	Sphere				Lens			
	Tensile (InAs/InSb)		Compressive (InAs/GaAs)		Tensile (InAs/InSb)		Compressive (InAs/GaAs)	
	Dot (InAs)	Matrix (InSb)	Dot (InAs)	Matrix (GaAs)	Dot (InAs)	Matrix (InSb)	Dot (InAs)	Matrix (GaAs)
Strain profile	$I > 0$ $B = 0$	Fast decay Slow decay	$I < 0$ $B = 0$	Fast decay Slow decay	$I > 0$ $B > 0$	Fast decay Slow decay	$I < 0$ $B > 0$	Fast decay Slow decay
Confining potential	$I > 0; E_g \downarrow$ $B = 0$	$B \neq 0$	$I < 0; E_g \uparrow$ $B = 0$	$B \neq 0$	$I > 0; E_g \downarrow$ $B \neq 0$	$B \neq 0$	$I < 0; E_g \uparrow$ $B \neq 0$	$B \neq 0$
	$V_{\text{HH}} = V_{\text{LH}}$	$V_{\text{HH}} > V_{\text{LH}}$	$V_{\text{HH}} = V_{\text{LH}}$	$V_{\text{HH}} < V_{\text{LH}}$	$V_{\text{HH}} < V_{\text{LH}}$	$V_{\text{HH}} > V_{\text{LH}}$	$V_{\text{HH}} > V_{\text{LH}}$	$V_{\text{HH}} < V_{\text{LH}}$
	V_{HH} has wings		V_{LH} has wings		V_{HH} has wings		no wings	

calculated strain profiles and confining potentials. We will refer to this tables as a guide for the remainder of this paper.

III. RESULTS

A. Strain profile

Figure 1 shows the strain profile of an embedded *sphere*, whereas Fig. 2 shows the corresponding strain for an embedded *lens*. As summarized in Table I, we see that (i) both sphere and lens-shaped dots have nonzero (and nearly constant) isotropic (I) strain *inside* the dot which rapidly decays to zero outside the dot. Naturally, tensile dots have $I > 0$, whereas compressed dots have $I < 0$. (ii) The biaxial strain (B) decays slowly to zero outside the dot. (iii) Spherical dots have $B = 0$ inside the dot, whereas lens-shaped dots have $B \neq 0$ inside the dot. The biaxial strain is positive in both tensile and compressive dots. The top left panel of Fig. 3 shows 3D rendering of the biaxial strain on the equatorial plane of the sphere and 1.5 nm above the base of the lens, better illustrating the angular dependence of the biaxial strain. Interestingly the biaxial strain has a nontrivial angular dependence. For the sphere, four maxima of B are seen along the [100] and [010] directions, and minima along the [110] and $[\bar{1}\bar{1}0]$ directions. This anisotropy is due to the underlying zinc blende lattice of the nanostructure and is missed by isotropic continuum elasticity. For the lens, no such maxima can be seen and the most prominent feature is a plateau throughout the lens that shows a large, almost constant, biaxial strain inside the dot.

Our forgoing results were obtained using *atomistic* elasticity (i.e., VFF). If, however, we restrict ourselves to isotropic continuum elasticity, the results for spherical dots can be derived analytically.³ Given the dot radius ρ_0 , Poisson's ratio ν and lattice mismatch ϵ_0 , and using spherical coordinates (ρ, θ, ϕ) , we have the following (following Ref. 3).

(a) Inside the sphere,

$$\epsilon_{\rho\rho} = \epsilon_{\theta\theta} = \epsilon_{\phi\phi} = \frac{2}{3}\epsilon_0 \frac{1-2\nu}{1-\nu} = \text{const.} \quad (1)$$

Here, ϵ_0 is the relative lattice mismatch, and $\nu = C_{12}/(C_{11} + C_{12})$. For InSb the elastic constants are¹⁸ $C_{11} = 685$ GPa and $C_{12} = 374$ GPa. The isotropic part of the strain is

$$I \equiv \epsilon_{\rho\rho} + \epsilon_{\theta\theta} + \epsilon_{\phi\phi} = 2\epsilon_0 \frac{1-2\nu}{1-\nu} \quad (2)$$

and biaxial part of strain is

$$B \equiv [(\epsilon_{\rho\rho} - \epsilon_{\theta\theta})^2 + (\epsilon_{\theta\theta} - \epsilon_{\phi\phi})^2 + (\epsilon_{\phi\phi} - \epsilon_{\rho\rho})^2]^{1/2} = 0. \quad (3)$$

(b) Outside the sphere,

$$\epsilon_{\rho\rho} = -2\epsilon_{\theta\theta} = -2\epsilon_{\phi\phi} = \frac{2}{3}\epsilon_0 \frac{1+\nu}{1-\nu} \left(\frac{\rho_0}{\rho}\right)^3 \sim \rho^{-3}, \quad (4)$$

where ρ_0 is the radius of the sphere. The isotropic part of the strain is $I = 0$, and the biaxial part is given by

$$B = \sqrt{2}|\epsilon_0| \left(\frac{\rho_0}{\rho}\right)^3 \sim \rho^{-3}. \quad (5)$$

Figure 1(a) gives the isotropic and biaxial strains calculated from continuum elasticity for an InAs/InSb dot with diameter $2R = 5.6$ nm, whereas Fig. 1(b) gives the atomistic results for the same dot. Comparing Figs. 1(a) and 1(b) we see

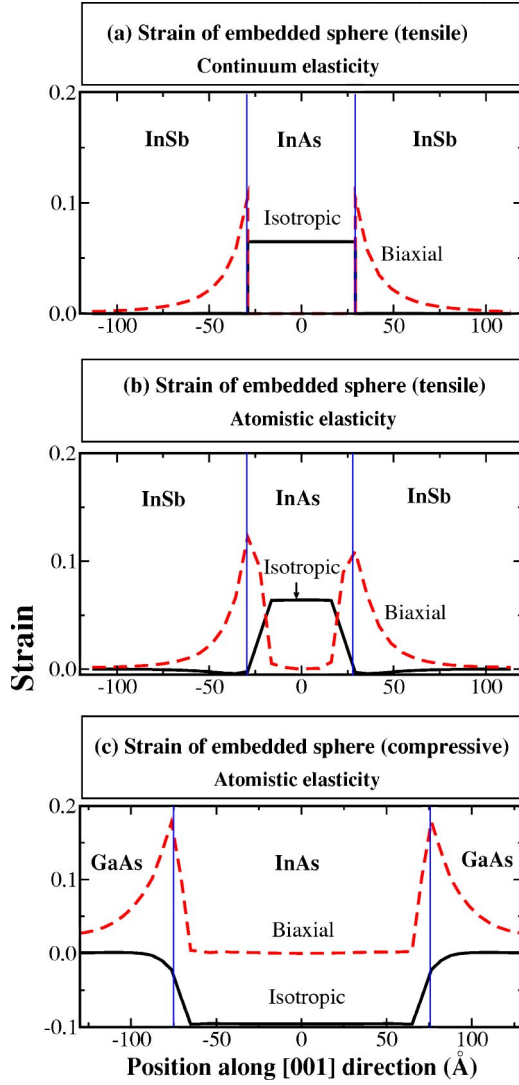


FIG. 1. (Color online.) Strain profiles for embedded spherical QD's along the [001] direction. (a) Results obtained assuming isotropic continuum elasticity (analytical), (b) atomistic strain from VFF, for tensile InAs/InSb QD's with diameter=5.6 nm, (c) atomistic strain from VFF for compressive InAs/GaAs QD's with diameter=13.6 nm. The thin vertical lines indicate the interface between the dots and their matrix materials.

that the atomistic and continuum elasticity results agree very well along the [001] direction (and along the equivalent [100] and [010] directions), except at the interface, where atomistic details are important.

Equation (5) can be tentatively used to estimate the strain profile outside the lens-shaped quantum dots in growth direction [001], whereas the lens is treated as a truncation from a sphere with effective radius $\rho_0 = (4h^2 + D^2)/8h$, and here D and h are the diameter and height of the lens, respectively. For flat dots with large effective radius ρ_0 one should expect a larger decay length of the biaxial strain in the barrier along the [001] growth direction. This is clearly seen when comparing the biaxial strain of a lens with a small effective radius of 6.5 nm [Fig. 2(b)] and that of a dots with a larger effective radius of 24.4 nm [Fig. 2(d)]. However, the differ-

ent magnitudes of B observed in the small lens [Fig. 2(b)] and in the large lens [Fig. 2(d)] cannot be accounted for by the analytic formula in Eq. (5) that gives a similar magnitude of B , since both systems have similar $|\epsilon_0|$. It is, however, expected that a flat dot will have smaller biaxial strain at the interface than a tall dot of the same material. In the limiting case of a thin film (infinite effective radius) embedded in a infinite barrier, the biaxial strain must be exactly zero in the barrier material.

B. Strain-modified potentials

Figure 4 shows the strain-modified confining potentials for LH, HH, SO (split off), and the electron ($e1$) bands for an embedded *sphere*, whereas Fig. 5 shows analogous results for an embedded *lens*. To obtain Figs. 4 and 5 we have used the simplified model of Pikus and Bir¹⁹ to account for strain effects. This model is, however, not used in our actual calculation of the single particle eigenstates, but serves only as illustration of strain effects. We followed the notation of Ref. 20, in which the model is written in real space. For the *conduction* band, the Hamiltonian is simply

$$H_c(\vec{\epsilon}) = a_c I \quad (6)$$

where a_c is the hydrostatic deformation potential of the conduction band and I is the isotropic strain. For *valence* bands (with spin-orbit coupling), the model Hamiltonian is

$$H_v(\vec{\epsilon}) = H^{SO} + a_v I - b_v \left[\begin{array}{c} \left(\begin{array}{ccc} -2 & 0 & 0 \\ 0 & 1 & 0 \\ 0 & 0 & 1 \end{array} \right) \epsilon_{xx} + \left(\begin{array}{ccc} 1 & 0 & 0 \\ 0 & -2 & 0 \\ 0 & 0 & 1 \end{array} \right) \epsilon_{yy} \\ + \left(\begin{array}{ccc} 1 & 0 & 0 \\ 0 & 1 & 0 \\ 0 & 0 & -2 \end{array} \right) \epsilon_{zz} \end{array} \right] - \sqrt{3} d_v \left[\begin{array}{c} \left(\begin{array}{ccc} 0 & -1 & 0 \\ -1 & 0 & 0 \\ 0 & 0 & 0 \end{array} \right) \epsilon_{xy} \\ + \left(\begin{array}{ccc} 0 & 0 & 0 \\ 0 & 0 & -1 \\ 0 & -1 & 0 \end{array} \right) \epsilon_{yz} + \left(\begin{array}{ccc} 0 & 0 & -1 \\ 0 & 0 & 0 \\ -1 & 0 & 0 \end{array} \right) \epsilon_{zx} \end{array} \right], \quad (7)$$

where, H^{SO} is the spin-orbit Hamiltonian,²⁰ a_v is the hydrostatic deformation potential of the VBM, b_v is the biaxial deformation potential of the VBM, and d_v is the deformation potential due to shear strain. The values of the deformation potentials a_c , a_v , and b_v for InAs, InSb, and GaAs are taken from Ref. 18. For [001] strain $\epsilon_{xx} = \epsilon_{yy} \neq \epsilon_{zz}$ and $\epsilon_{xy} = \epsilon_{yz} = \epsilon_{zx} = 0$. In this case, Eq. (7) can be simplified to

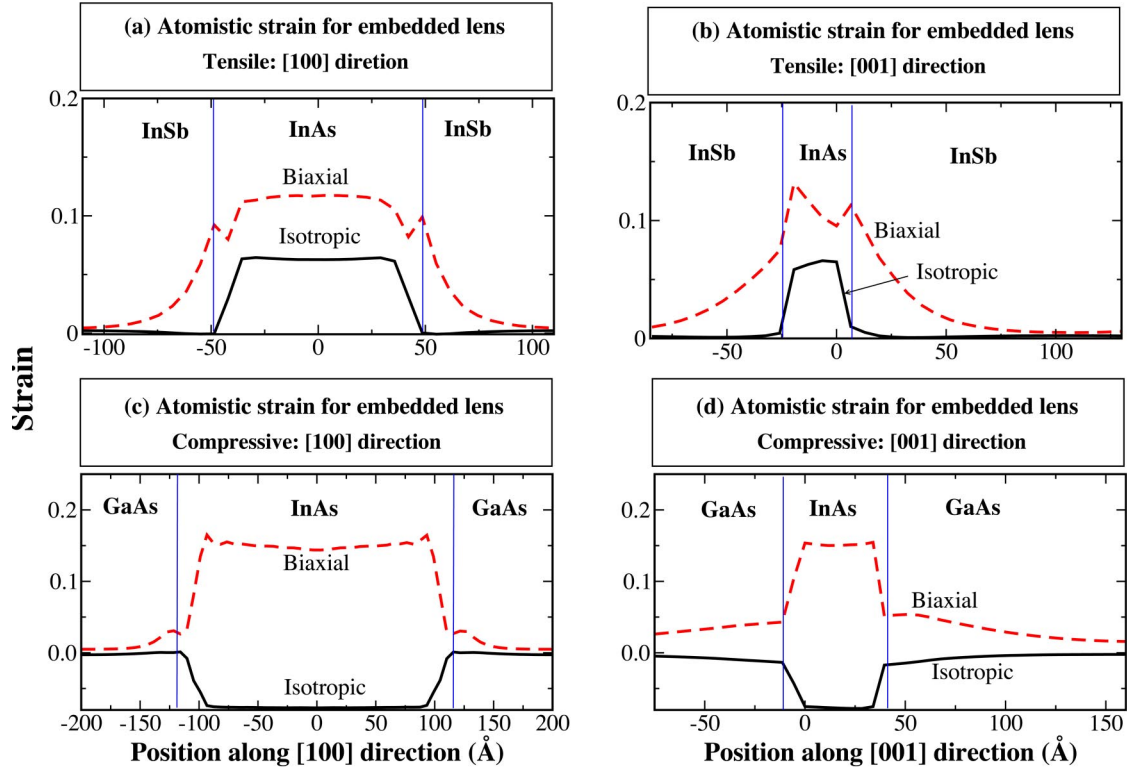


FIG. 2. (Color online.) Strain profiles for embedded lens-shaped QD's: Panels (a) and (b) give the strain profiles of a lens-shaped InAs/InSb QD ($10.4 \text{ nm} \times 2.6 \text{ nm}$), (a) along [100] direction and (b) along [001] direction. Panels (c) and (d), give the strain profiles of a lens-shaped InAs/GaAs QD ($25 \text{ nm} \times 3.5 \text{ nm}$), (c) along [100] direction and (d) along [001] direction. The biaxial strain outside the lens in (d) decays much slower than in (b), because (d) has a larger effective radius (see text).

$$H_v(\vec{\epsilon}) = H^{SO} + a_v I - \Delta_{001}(\vec{\epsilon}) \begin{pmatrix} 1 & 0 & 0 \\ 0 & 1 & 0 \\ 0 & 0 & -2 \end{pmatrix}, \quad (8)$$

where $\Delta_{001} = b_v[\epsilon_{zz} - \epsilon_{xx}]$ is the heavy- or light-hole splitting or crystal-field splitting. The eigenvalues of this equation give the energy of the three valence bands VB1, VB2, and VB3 in decreasing order of energy. The strain-modified confining potential shown in Figs. 4 and 5 is obtained by solving Eq. (7) in real space at each eight-atom unit cell using the local strain input from VFF.

To analyze the valence confining potentials obtained from Eq. (7) in terms of their HH, LH and SO character, we project the eigenfunctions to the HH, LH, and SO basis sets, i.e., $|J, J_z\rangle = \{|3/2, \pm 3/2\rangle, |3/2, \pm 1/2\rangle, |1/2, \pm 1/2\rangle\}$, respectively. The dominant character of each band is marked in Figs. 4 and 5 as “HH,” “LH,” “SO,” and “e1” for conduction band character. Typically, the HH, LH character of a band changes from the inside to the outside of the nanostructure, e.g., a band with HH character outside the dot has LH character inside, and vice versa. The salient features of Figs. 4 and 5 (as summarized in Table I) are as follows.

1. The effect of isotropic strain on potentials

The isotropic strain (Figs. 1 and 2) has the same effect on the potential (Figs. 4 and 5) of spherical and lens-shaped

dots: namely, for tensile dots (InAs/InSb), the potential of InAs V_{CBM} and V_{VBM} are both *lowered*, but the InAs CBM is lowered faster, leading to an overall *reduction* of the gap, whereas for compressive dots (InAs/GaAs) the potential of InAs V_{CBM} and V_{VBM} are both *raised*, but the InAs CBM is raised faster, leading to an overall *increase* of the gap.

2. The effect of biaxial strain on potentials

The biaxial strain B (Figs. 1 and 2) of spherical and lens-shaped dots is reflected in the potentials.

(a) For *spherical* dots, B is zero inside the sphere and therefore $V_{\text{LH}} = V_{\text{HH}}$ leading to degenerate HH and LH states, no matter how large the mismatch strain is. Outside the dots, $B \neq 0$, leading to the splitting of HH and LH states. It should be noted, that although the biaxial strain B is identical in the [001], [100], and [010] directions, the HH and LH character of the bands is different for each of these directions. This is intrinsic to the choice one has to make when defining the basis states HH, LH, and SO. In this paper, we choose the [001] direction as z axis and restrict our discussion of HH/LH characters along this axis unless indicated otherwise. Along the [001] direction, we find for tensile strain $V_{\text{HH}} > V_{\text{LH}}$ (i.e., holes prefer the HH state) outside the sphere, while for compressive strain $V_{\text{HH}} < V_{\text{LH}}$ (i.e., holes prefer LH state). Along any other direction than [001], the confining potentials have mixed HH and LH characters. In Fig. 3 the confining potentials of the first conduction band CB and the

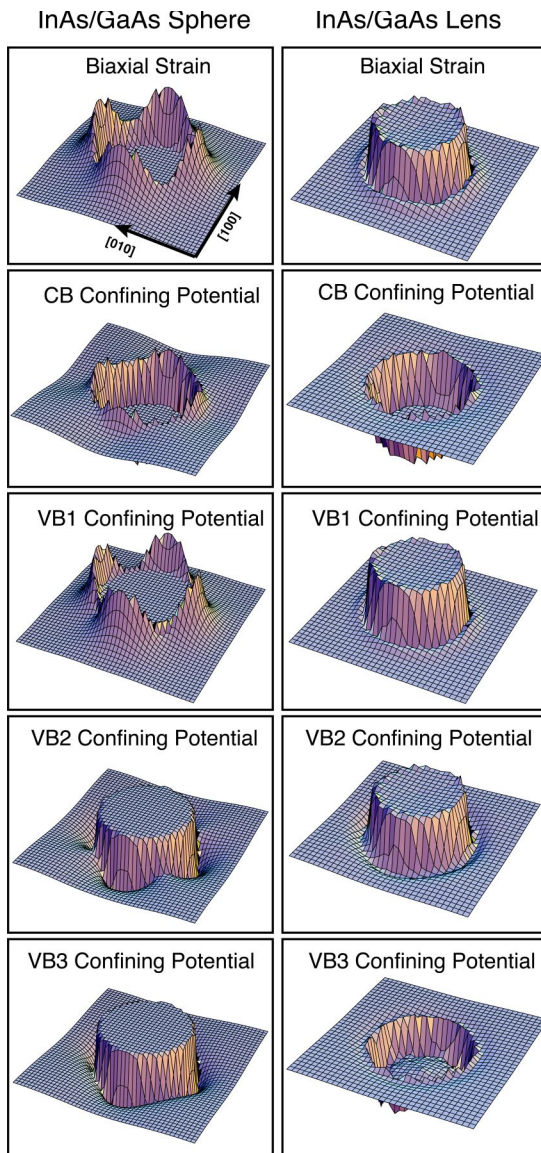


FIG. 3. Biaxial strain (top panels), conduction band (CB), and valence band (VB1, VB2, VB3) confining potentials for a spherical InAs/GaAs QD with 13.6 nm diameter (left panels) and for a lens shape InAs/GaAs QD with 25 nm base and 3.5 nm height (right panels). The plots show a 3D rendering of the equatorial (001) plane for the sphere and a plane 1.5 nm above the base of the dot for the lens.

first three valence bands VB1, VB2, and VB3 are given for the equatorial plane of the sphere. The first valence band resembles the biaxial strain with significant maxima along the [100] and [010] directions and minima along the [110] and $[\bar{1}\bar{1}0]$ directions.

(b) For *lens-shaped* dots, $B \neq 0$ even *inside* the nanostructure and therefore $V_{HH} \neq V_{LH}$ leading to a splitting of the HH and LH states and the reversal of their order inside and outside the dot. This is seen clearly for example for lens-shaped tensile (InAs/InSb) dot in Fig. 6, which decomposes each confining potential along the [001] direction into HH, LH, SO character. We see that the hole states have distinct (although somewhat mixed) confining potentials: in *tensile* dots

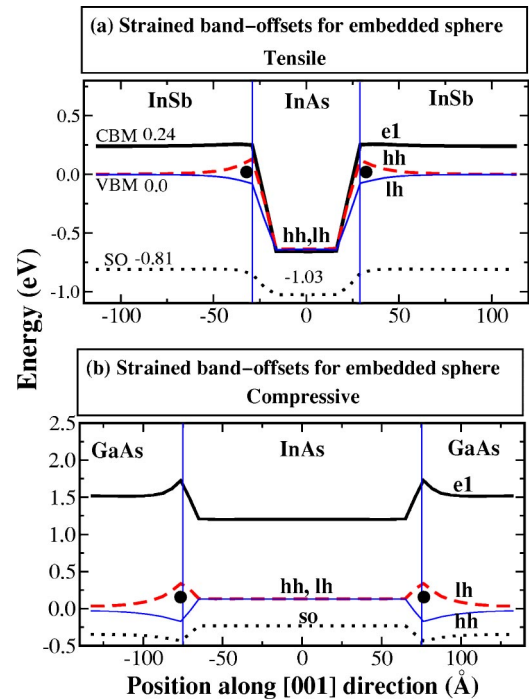


FIG. 4. (Color online.) Strain-modified confining potentials of embedded spheres calculated from Eqs. (7) and (8) for (a) tensile strain (InAs/InSb) and (b) compressive strain (InAs/GaAs). The HH and LH bands are degenerate inside the dots, but split outside. The numbers next to CBM, VBM, and SO, are in eV with the VBM of InSb taken as reference energy. The possible hole traps are indicated by the solid circles.

the first hole confining potential is LH inside the dot and HH outside the dot, whereas the second hole potential is just the reverse (HH inside the dot and LH outside the dot); in *compressive* dots (not shown), the first hole potential is HH inside and LH outside, whereas the second hole potential is LH inside and HH outside. The third hole potential is SO both inside and outside in all cases. The HH, LH splitting has opposite sign in the tensile (InAs/InSb) and the compressive (InAs/GaAs) case due to the sign difference in the $\epsilon_{zz} - \epsilon_{xx}$ [Eq. (8)] term. Similarly to the case of spherical dots the band characters along the [100] and [010] directions are mixed HH and LH. On the right panels of Fig. 3 the confining potentials of the first conduction band CB and the first three valence bands VB1, VB2, and VB3 are given for a plane 1.5 nm above the base of a lens shaped dot with 25 nm base and 3.5 nm height. The first valence band resembles again (as in the sphere) the biaxial strain with a significant plateau inside the nanostructure.

3. Hole localization at the interface

(a) In *spherical* dots, the biaxial strain outside the dot, close to the interface, leads to a localizing piece of VB1 (that has HH character along [001] in InAs/InSb and LH character along [001] in InAs/GaAs)—distinctly visible as peaks in the left panels of Fig. 3 and highlighted in Fig. 4 as solid circles—which could trap holes. Specifically, the “wing feature” of the biaxial strain in the barrier splits HH and LH

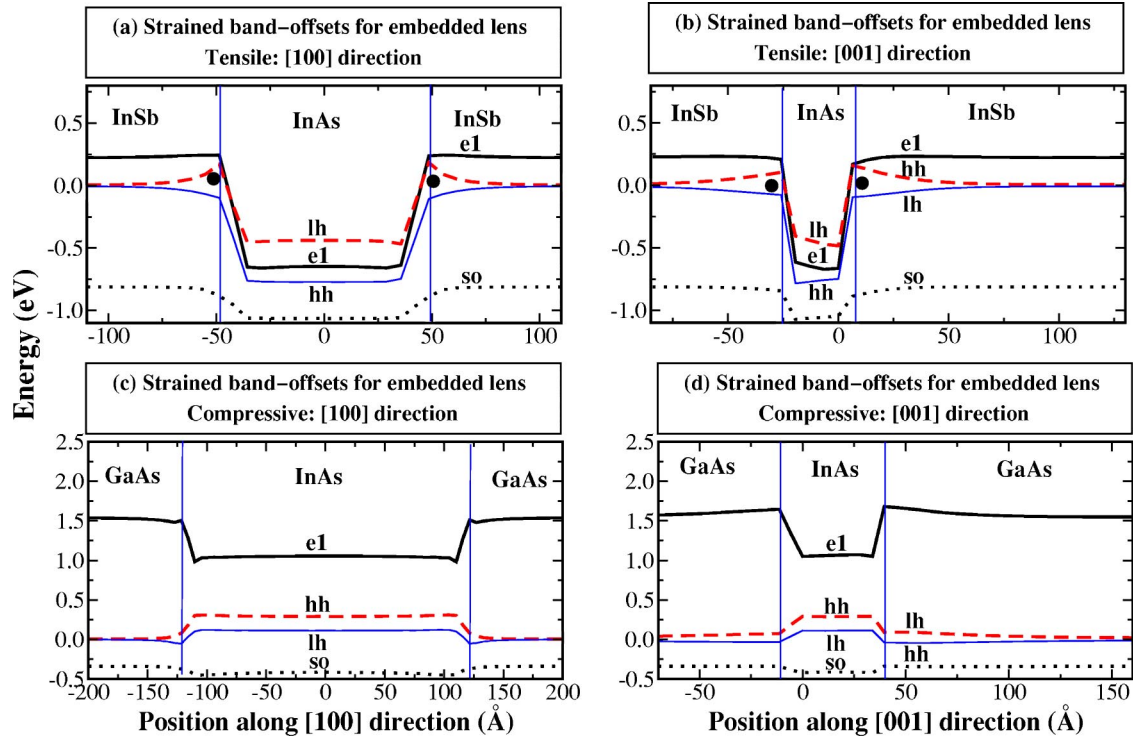


FIG. 5. (Color online.) Strain-modified confining potentials of lens-shaped QD's calculated from Eqs. (7) and (8) for (a) tensile strain (InAs/InSb) along [100] direction, (b) tensile strain (InAs/InSb) along [001] direction, (c) compressive strain (InAs/GaAs) along [100] direction, and (d) compressive strain (InAs/GaAs) along [001] direction. For the first (dashed line) and second (thin solid line) hole confining potentials, the HH, LH characters are reversed inside and outside the dots along the [001] direction. Along the [100] direction, the character of these first two hole potentials outside the dots is HH and LH mixed and no label has been assigned to them in the figure.

potentials raising one up (HH in InSb and LH in GaAs, along the [001] direction) to reach a maximum value at the interface in the $\langle 100 \rangle$ directions. If this potential maximum is energetically higher than the hole confining potential inside the dots and has sufficient extent in real space, the holes will then prefer to localize in these “pockets.”

(b) *Lens-shaped* dots: The same features as observed for the spheres can be seen for the lens-shaped tensile InAs/InSb dots [Figs. 5(a) and 5(b)] where possible hole localization is marked as solid circles. However, unlike the case in spherical dots, no “hole trap” is observed in a lens-shaped InAs/GaAs dots of 25 nm base and 3.5 nm height (right panels of Fig. 3). The difference between spherical and lens-shaped InAs/GaAs QD's is that, in spherical dots, there is no biaxial strain inside InAs, and the V_{HH} and V_{LH} potentials of InAs are energetically lower (less favorable for holes) than the V_{LH} of GaAs [see Fig. 4(b)], so holes prefer to localize on the interface. However, as shown in Figs. 5(c) and 5(d), the biaxial strain inside the lens raises the V_{HH} in InAs energetically higher (more favorable for holes) than the V_{LH} in GaAs in the barrier, thus holes prefer to localize on V_{HH} inside InAs rather than being trapped at the interface.

C. Wave functions of confined states

To assess the validity of the qualitative observations we made we studied the confined electron and hole levels and

their wave functions using the atomistic pseudopotential methods. For InAs/InSb QD's, a spherical dot with diameter=5.6 nm, and a lens-shaped dot with base \times height =10.4 \times 2.6 nm have both only one electron state confined inside the dot and six hole states localized on the dot interface. For InAs/GaAs QD's, a spherical dot with diameter =13.6 nm, and a lens-shaped dot with dimension=25 \times 3.5 nm dot have both more than 10 electron and 10 hole states confined inside the dot. For the spherical dots of T_d atomistic symmetry,¹⁶ one expects three degenerated electron P states that will be slightly split into a doublet and a singlet by spin-orbit interaction. For the lens-shaped dot of C_{2v} symmetry with inequivalent [110] and $[1\bar{1}0]$ directions (arising from atomistic considerations, even for a cylindrically shaped quantum dot), the doublet splits further into two singlet and no more degeneracy remains, other than the Kramers spin degeneracy that can be lifted by magnetic fields.

In Figs. 7 and 8, for lens shaped and spherical dots, respectively, we show the isosurfaces of the square of the wave functions for the first three hole states h_0, h_1, h_2 and the first three electron states e_0, e_1, e_2 for the InAs/GaAs and the InAs/InSb dots. The isosurfaces enclose 75% (25%) of the states density for the InAs/GaAs (InAs/InSb) dot. The dimensions of the spheres are shown as half spheres and the dimension of the lenses are shown as gray surfaces.

a. Wave functions in the sphere. The hole states are all localized around the interface, mostly along the [001], [010],

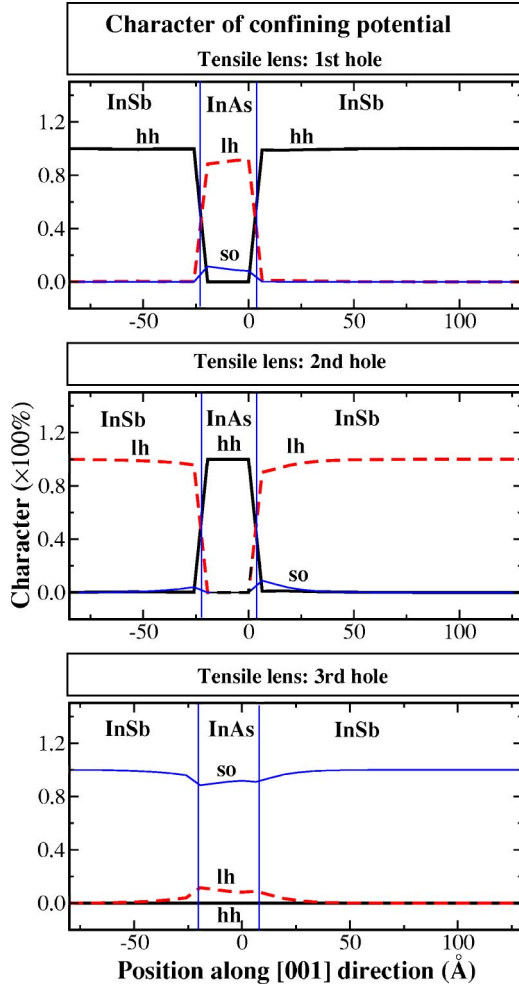


FIG. 6. (Color online.) Decomposed HH (thick solid line), LH (dashed line), and SO (thin solid line) character of the (a) first, (b) second, and (c) third hole confining potentials for lens-shaped InAs/InSb QD's.

and [100] directions, for both type III InAs/InSb and type I InAs/GaAs QDs. This hole localization was suggested by the stain-modified band offset results of Sec. III B and is a consequence of the effect of biaxial strain on the first hole confining potential, as seen on the left of Fig. 3. We further note that no hole localization at the interface was found in

small spherical InAs/GaAs dots with 4.2 nm diameter in Ref. 21.

b. Wave functions in the lens. The wave functions of the lens-shaped InAs/GaAs and InAs/InSb dots are given in Fig. 8 for the first few electron and hole states in the same fashion they were shown for the sphere in Fig. 7. The type I InAs/GaAs flat lens shows localized states inside the nanostructure and, as was suggested by Fig. 3, no hole localization at the interface is seen.

c. Wave function decomposition. To get more information about the detailed character of the confined states, we project again the single-particle eigenfunctions obtained from our pseudopotential calculations onto the HH, LH, and SO basis sets $|J, J_z\rangle$ and decompose them into their angular momentum components. For the InAs/InSb dots, the weak confinement potential (compared to InAs/GaAs) let the electron and hole states leak out of (for the electron) and leak in (for holes) the nanostructures making the analysis less conclusive. The results are therefore only shown for the InAs/GaAs dots in Table II. For the spherical InAs/GaAs dots the confined hole states have equal HH and LH characters due to the equivalence of the x , y , and z directions in T_d symmetry, while in the lens-shaped dot, the confined hole states have dominantly HH character, as expected from the strained modified band offset analysis: the HH band is pushed up in energy through biaxial strain. The confined electron levels in the lens and the sphere have 85–92 % conduction band character and are dominated by a single angular momentum component (S, P, D , etc.). Similar results, with almost pure angular momentum character, are found for the hole states in lens-shaped InAs/GaAs dots. However, the hole states in spherical InAs/GaAs dots, which are confined at “the corners” of the interface along the [001], [010], and [100] directions have mixed angular momentum components and Bloch function characters as listed in Table II.

IV. SUMMARY

We compared the shape effects (sphere vs lens) on tensile (InAs/InSb) and compressive (InAs/GaAs) matrix-embedded QD's. Our results show that for the QD's, the biaxial strain, as a consequence of the dot shape, is a function of position, decaying with distance away from the interface. We further show that the position-dependent strain controls the HH, LH degeneracy, reverses their order inside and

TABLE II. Angular momentum (S, P, D , etc.) and Bloch function (e, HH, LH, SO) character of the first three confined electron and hole states in a spherical (diameter=13.6 nm) and a lens-shaped (diameter=25 nm, height=3.5 nm) InAs/GaAs QD's.

State	Sphere		Lens	
	Character	Type of state	Character	Type of state
e_0	$S(91\%)$	$e(92\%)$	$S(85\%)$	$e(88\%)$
e_1	$P(85\%)$	$e(87\%)$	$P(83\%)$	$e(85\%)$
e_3	$P(85\%)$	$e(87\%)$	$P(83\%)$	$e(86\%)$
h_0	$D(35\%)+G(18\%)$	$HH=LH(44\%)$	$S(92\%)$	$HH(91\%)$
h_1	$F(40\%)$	$HH=LH(44\%)$	$P(86\%)$	$HH(86\%)$
h_2	$D(19\%)+F(22\%)+G(19\%)$	$HH=LH(44\%)$	$P(86\%)$	$HH(92\%)$

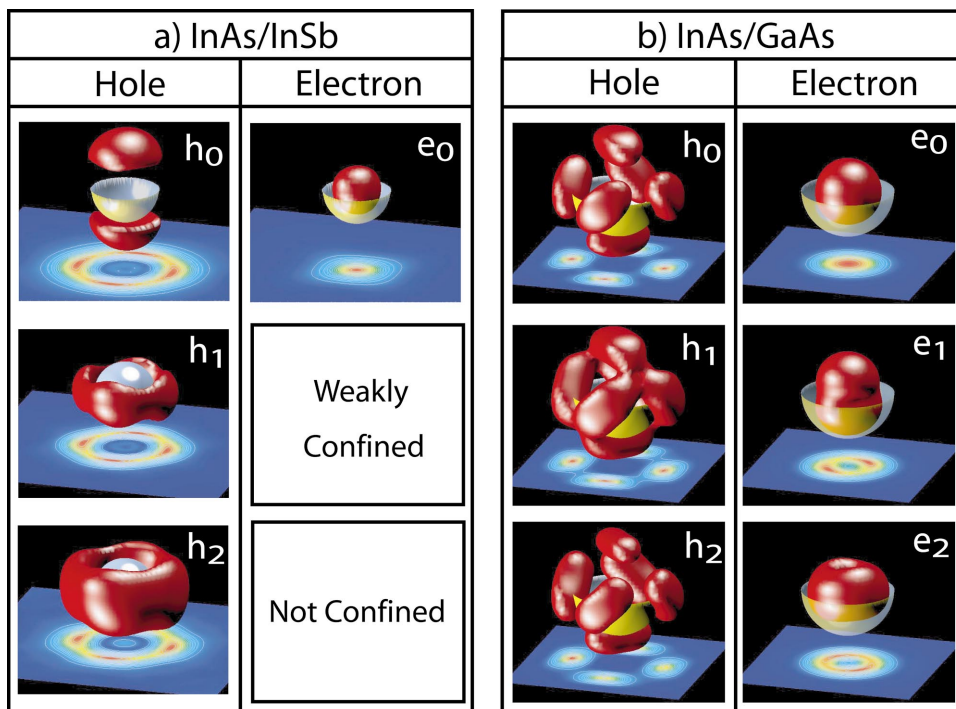


FIG. 7. (Color.) Square of the wave functions for spherical (a) InAs/InSb (diameter=5.6 nm) and (b) InAs/GaAs QD's (diameter =13.6 nm). The half spheres indicate the position of the dots and the isosurfaces enclose 75% of the state density for the InAs/GaAs dot and 25% of the state density for the InAs/InSb dot. The contour plots are slices of the density taken through the middle of the spheres. We show the first three electron and first three hole states except for the InAs/InSb QD where only one electron level is well confined.

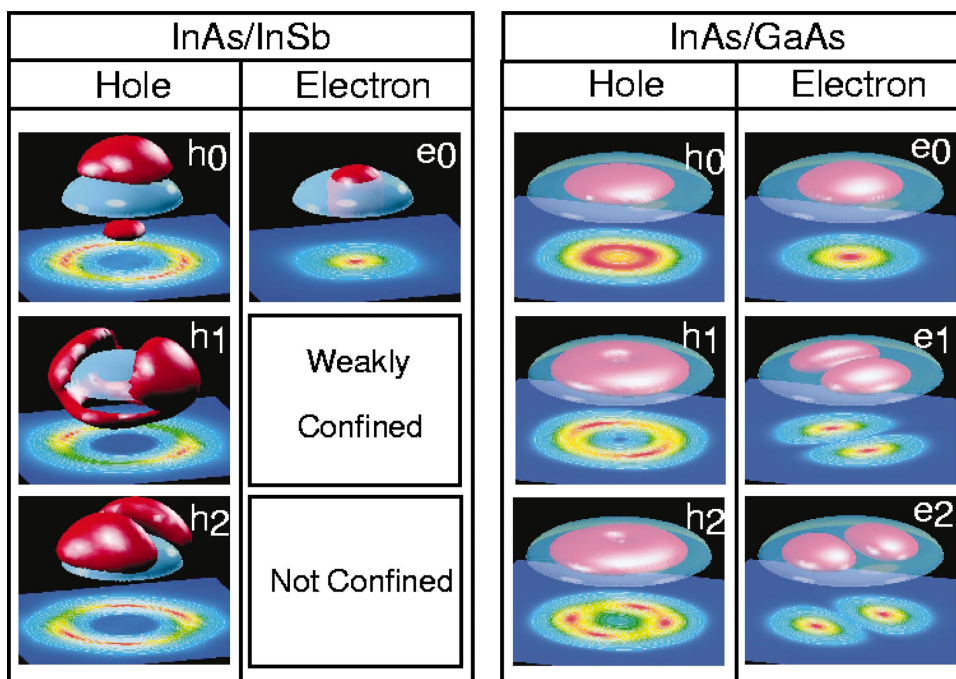


FIG. 8. (Color.) Equivalent to Fig. 7 but for lens-shaped InAs/InSb (10.4 nm×2.6 nm) and InAs/GaSb (25 nm×3.5 nm) quantum dots. The contour plots are slices of the density taken 1 nm above the base of the lenses.

outside the dots, and leads to interfacial hole localization. For InAs/InSb QD's, where the VBM of the barrier is higher than the VBM of the dots, interfacial hole localization is found for both spherical and lens-shaped dots. However, for type I InAs/GaAs QD's, where the VBM of the barrier is lower than the VBM of the dots, interfacial hole localization is only found in the spherical and tall lens shaped dots while in *flat* lens-shaped dots, holes are confined inside the dot. Hole localization has obvious consequences on optical properties of the QD's, e.g., for type I systems, the interfacial hole localization will *reduce* optical activity and prolong exciton lifetime. Thus, for flat dots, with electron and hole states localized inside the nanostructure we expect strong oscillator strength typical of an *S-S* interband transition. With increasing dot height and aspect ratio we expect a reduced

absorption and emission typical of *S-P* transitions. With the change of state-character we furthermore expect a change in polarization as a function of dot height. On the contrary, for type II quantum dots, interfacial hole localization will *increase* optical activity. For type III systems (e.g., InAs/InSb QD's), hole localization at the interface may enhance the exciton binding energy and may lead to a novel excitonic ground state at certain dot sizes.²²

ACKNOWLEDGMENTS

We would like to thank R. Goldman for bringing our attention to Ref. 7. This work was supported by US DOE-SC-BES-DMS.

*Electronic address: alex_zunger@nrel.gov

¹*Interfaces, Quantum Wells, and Superlattices*, edited by C. R. Leavens and R. Taylor (Plenum Press, New York, 1987).

²*Quantum Well Intersubband Transition Physics and Devices*, edited by H. C. Liu, B. F. Levine, and J. Y. Andersson (Kluwer, Dordrecht, 1993).

³D. Bimberg, M. Grundmann, and N. N. Ledentsov, *Quantum Dot Heterostructures* (Wiley, New York, 1999).

⁴C. Pryor, J. Kim, L.-W. Wang, A. J. Williamson, and A. Zunger, *J. Appl. Phys.* **83**, 2548 (1998).

⁵A. J. Williamson, A. Zunger, and A. Canning, *Phys. Rev. B* **57**, R4253 (1998).

⁶L.-W. Wang, *Phys. Rev. B* **63**, 245107 (2001).

⁷M. Pinczolits, G. Springholz, and G. Bauer, *Appl. Phys. Lett.* **73**, 250 (1998).

⁸A. Henglein, *Chem. Rev. (Washington, D.C.)* **89**, 1861 (1998).

⁹L. Brus, *J. Phys. Chem. Solids* **59**, 459 (1998).

¹⁰P. N. Keating, *Phys. Rev.* **145**, 637 (1966).

¹¹A. J. Williamson, L.-W. Wang, and A. Zunger, *Phys. Rev. B* **62**, 12 963 (2000).

¹²R. Magri and A. Zunger, *Phys. Rev. B* **65**, 165302 (2002).

¹³L.-W. Wang and A. Zunger, *Phys. Rev. B* **59**, 15 806 (1999).

¹⁴H. Fu, L.-W. Wang, and A. Zunger, *Appl. Phys. Lett.* **71**, 3433 (1997).

¹⁵L.-W. Wang, A. J. Williamson, A. Zunger, H. Jiang, and J. Singh, *Appl. Phys. Lett.* **76**, 339 (2000).

¹⁶A. Zunger, *Phys. Status Solidi A* **190**, 467 (2002).

¹⁷The InSb pseudopotentials are revised to reproduce the correct band-offset of the InSb VBM relative to the VBM of GaSb, changing it from 40 meV below the GaSb VBM to 34 meV above, according to the experimental findings of Ref. 18. R. Magri, A. Zunger, and H. Krower (unpublished).

¹⁸I. Vurgaftman, J. R. Meyer, and L. R. Ram-Mohan, *J. Appl. Phys.* **89**, 5815 (2001).

¹⁹G. E. Pikus and G. L. Bir, *Fiz. Tverd. Tela (Leningrad)* **1**, 154 (1959) [*Sov. Phys. Solid State* **1**, 136 (1959)]; **1**, 1642 (1959) [**1**, 1502 (1959)]; **3**, 1001 (1961) [**3**, 730 (1961)]; *Phys. Rev. Lett.* **6**, 103 (1961).

²⁰S.-H. Wei and A. Zunger, *Phys. Rev. B* **49**, 14 337 (1994).

²¹A. J. Williamson and A. Zunger, *Phys. Rev. B* **59**, 15 819 (1999).

²²L. He, G. Bester, and A. Zunger, *Phys. Rev. Lett.* (to be published).